PAPER • OPEN ACCESS

Magnetic hyperthermia application of MnFe$_2$O$_4$ nanostructures processed through solvents with the varying boiling point

To cite this article: R K Chandunika *et al* 2020 *Mater. Res. Express* **7** 064002

View the article online for updates and enhancements.

Materials Research Express

PAPER

Magnetic hyperthermia application of MnFe$_2$O$_4$ nanostructures processed through solvents with the varying boiling point

R K Chandunika[1], R Vijayaraghavan[2] and Niroj Kumar Sahu[1,3]

[1] Centre for Nanotechnology Research, Vellore Institute of Technology, Vellore-632014, Tamil Nadu, India
[2] School of Advance Sciences, Vellore Institute of Technology, Vellore-632014, Tamil Nadu, India
[3] Author to whom any correspondence should be addressed.

E-mail: rk.chandunika@gmail.com, rvijayaraghavan@vit.ac.in and nirojs@vit.ac.in

Abstract

This article reports the synthesis of MnFe$_2$O$_4$ nanoparticles (NPs) by thermal decomposition method in different solvents such as diphenyl ether, benzyl ether and 1-octadecene with varying boiling point (bp). The physical and chemical properties of all the NPs were systematically studied. The NPs prepared using benzyl ether as solvent formed in cubic shape whereas spherical particles are formed in diphenyl ether and 1-octadecene. The solvent plays a significant role in the reaction and influence the morphology of the NPs. The hydrophobic particles are made hydrophilic by ligand exchange using tetramethyl-ammonium 11-aminoundecanote and the colloidal dispersion of the NPs are used for magnetic induction in varying alternating magnetic field (AMF) of frequency 314 kHz. The specific absorption rates that measure the heat generation in NPs are found to vary with the concentration of the NPs as well as the field strength. The cubic shaped NPs shows comparatively better SAR than the spherical NPs.

1. Introduction

The synthesis of inorganic NPs are of tremendous interest in the past two decades due to their distinct properties compared to the bulk analogue useful in a wide range of applications. Now a days many researches have been carried out to study the relation between variations in morphology to their physicochemical properties. In recent years, many studies are reported related to different size and shapes of inorganic metal, metal oxides and semiconductor NPs [1–6]. For biomedical applications, magnetic particles among inorganic NPs are highly interested particularly for drug delivery, magnetic resonance imaging and hyperthermia [7–13]. Magnetic ferrites have unique magnetic, optical, electronic and catalytic properties due to their spinel structure (AB$_2$O$_4$) where A and B are tetrahedral and octahedral cation sites and O denotes the oxygen in anion sites. The spinel ferrites have face centred cubic structure with molecular formula MFe$_2$O$_4$ (M = Fe, Mn, Ni, Zn, Co or Mg). Among ferrites, MnFe$_2$O$_4$ can provide better biocompatibility and strong magnetisation for biomedical applications. Kim *et al* showed that MnFe$_2$O$_4$ among other metal ion-doped ferrites provide better contrast agent for MRI [14]. In clinical studies for hepatic MRI, Mn^{2+} containing contrast agent mangafodipir trisodium (MnDPDP, Teslascan) has been used [15]. By tuning the chemical composition, size and shapes of the magnetic NPs, the magnetic properties can be controlled. To get the desired physical and chemical properties of spinel ferrite, different chemical synthesis route has been the main focus of research. Different reported methods for the synthesis of magnetic NPs are ball milling, coprecipitation, sol-gel, hydrothermal, microwave-assisted route, microemulsion and thermal decomposition method. Different shapes of the NPs have been achieved by most of these methods but controlling the uniformity in large scale production is difficult. In this regard, the method involving decomposing of organometallic precursors in organic solvents shows better results in controlling the morphology of NPs when synthesized in large scale [16]. This fine-tune of sizes and shapes by thermal decomposition can be explained via the nucleation-growth theory proposed by Lamer [17]. The clear separation between nucleation and growth phase can be seen in the thermal decomposition method. The precursors

generally used in thermal decomposition methods are oleates [16, 18, 19], acetates [20] and acetylacetonates [21, 22]. The high-quality Fe_3O_4 NPs can be produced by the thermal decomposition method with high magnetic saturation value [23]. In this method, oleic acid and oleylamine were used as surfactants which play a major role in the morphological formation. In general, surfactants are used to prevent aggregation by forming a coating on the particle results in the uniform growth size of the particles. For the nucleation process, these surfactants can also act as a reducing agent. The amine and carboxylic acid based surfactants can accelerate or delay the decomposition rate of precursors [24].

On the other hand, the solvent also plays an important role on the NP formation by thermal decomposition method. Lu *et al* [25] studied the effect of reducing agent and solvent on the synthesis of $CoFe_2O_4$ NPs. They have presented the surfactant effect by changing the oleic acid and oleylamine in the equimolar concentration of 248 mM, 496 mM, and 620 mM keeping the same solvent and vice versa. The results show that the morphology $CoFe_2O_4$ NPs varies from spherical to cubes to star shape with increase in surfactant to solvent ratio when synthesized using dioctyl ether (bp = 287 °C) as a solvent, whereas the NPs formed only in spherical shapes of different size when synthesized in 1-octadecene (bp = 320 °C) with different surfactant ratio. Sun and co-workers [22] have reported the synthesis of MFe_2O_4 NPs by thermal decomposition method using different solvents. They reported the formation of two different sizes of NPs e.g. 4 and 6 nm by using phenyl and benzyl ether as solvents respectively keeping all other parameters same. The increase in NP size is concluded due to increase in the bp from 259 °C for phenyl ether to 298 °C for benzyl ether and inferred that the reaction temperature played significant role. Similarly, Zhou *et al* [26] demonstrated the controlled synthesis of anisotropic iron oxide nanoparticles in two different solvents 1-octadecene (bp = 320 °C) and tri-n-octylamine (bp = 360 °C) by changing the precursor ratios. From the series of synthesis, the one with precursor ratio of 1 mmol of iron oleate, 0.2 mmol of sodium oleate and 0.5 mmol of oleic acid in 1-octadecene as solvent produces iron oxide of truncated octahedron shape whereas in tri-n-octylamine solvent it formed in concave shapes. In the same report by Zhou *et al* cubic shaped iron oxide was synthesized in tri-n-octylamine as solvent without sodium oleate and reasoned that tri-n-octylamine act similar role as surfactant sodium oleate to deprotonate oleic acid from oleate (OL^-). Erik *et al* [27] reported synthesis of spherical and cubic shapes of iron oxide NPs using three different solvents 1-octadecene, 1-hexadecene (bp = 287 °C) and eicosane (bp = 343 °C) where the the reaction temperature play important role for variation in morphology of NPs. Park *et al* [16] reported ultra-large scale synthesis of monodispersed iron oxide NPs by thermal decomposition method of iron oleate precursor in high bp solvents such as 1-hexadecene, octyl ether, 1-octadecene, 1-eicosene and trioctylamine. The nanocrystals are highly monodisperse in nature and the variation in particle-size are reported due to variaton in the reaction temperature. There are many literatures published on the formation magnetic NPs by thermal decomposition method where the temperature of the reaction and surfactant used play significant role in the morphology of NPs, however, the solvents role on the particle size and shape of NPs has not yet been clearly established [26, 28–30].

In this present work, $MnFe_2O_4$ NPs are synthesized via a thermal decomposition method with three different solvents. The physico-chemical properties has been analysed through various characterisation techniques such as XRD, FESEM, XPS, TGA and VSM. The mechanism of morphological evolution in NPs have been explained and magneto-thermal induction capabilities $MnFe_2O_4$ colloid has been assessed with the application of AMF.

2. Materials and methods

2.1. Chemicals used
Manganese (II) acetylacetonate ($Mn(acac)_2$, 99%), iron (III) acetylacetonate ($Fe(acac)_3$, 99.99%), diphenyl ether (99%, bp: 258 °C), benzyl ether (90%, bp: 295 °C), 1-Octadecene (90%, bp: 320 °C), oleic acid (OA, 99%), oleylamine (OLA, 70%), absolute ethanol (99.99%), hexane (98.5%) were purchased from Sigma-Aldrich. All chemicals were of analytical grade and used without any purification.

2.2. Method used
Manganese ferrite was synthesized using a modified thermal decomposition method [22]. In a typical synthesis, 1 mmol of $Mn(acac)_2$, 2 mmol of $Fe(acac)_3$, 10 mmol of oleylamine and oleic acid and 20 ml of solvent were magnetically stirred under a nitrogen atmosphere as shown in scheme-1. The solvents used were either diphenyl ether (PE) or 1-octadecene (ODC) or benzyl ether (BE) and the prepared $MnFe_2O_4$ nanoparticles were named as MnF-PE, MnF-ODC, MnF-BE respectively. The solution was heated for 100 °C under a nitrogen blanket for 30 min to remove moisture and impurities in the solvents used. Then, the temperature was increased to 200 °C and maintained for another 30 min for nucleation. Followed by this, the temperature was increased to the boiling point of the solvent with the ramping rate of 3° per min and maintained for 60 min. After this, the
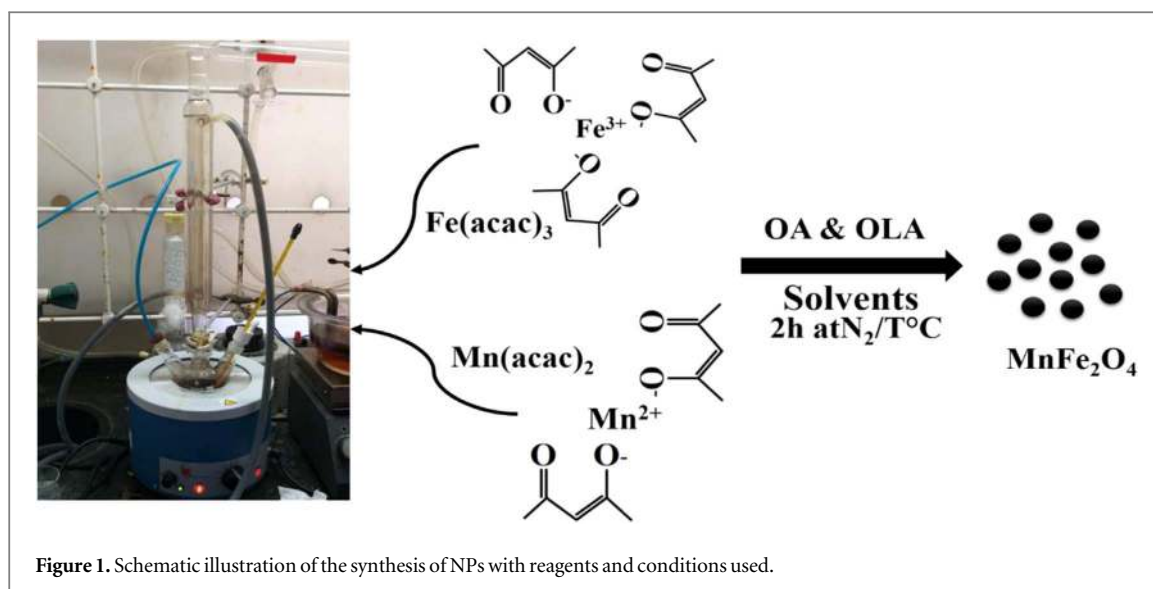
Figure 1. Schematic illustration of the synthesis of NPs with reagents and conditions used.

reaction vessel containing the NPs are cooled down to room temperature under N_2 blanket. The dark black precipitate was collected using centrifugation method. Ethanol was added to the solvent to form precipitation and then centrifuged at 7000 rpm for 15 min. The collected precipitate was redispersed in 5 ml of hexane and centrifuged again by adding ethanol and it was repeated for 3 times. The final product was dispersed in hexane and stored. To make the particles water soluble, 2 ml of hexane dispersed NPs was mixed with 2 ml of 20 mg tetramethyl-ammonium 11-aminoundecanote in dichloromethane [22]. The mixture was sonicated for 2 min and the particles were isolated using a permanent magnet and redispersed in water. The thermal decomposition of $Fe(acac)_3$ and $Mn(acac)_2$ produce $MnFe_2O_4$ in the presence of oleylamine and oleic acid as a surfactant in high boiling point solvent by releasing carbon dioxide and acetone byproducts as follows (1):

$$Fe(C_5H_7O_2)_3 + Mn(C_5H_7O_2)_2 \rightarrow MnFe_2O_4 + CH_3COCH_3 + CO_2 \qquad (1)$$
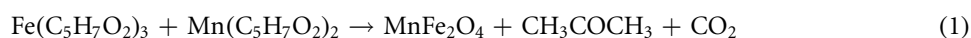
It is well known that the reaction parameters like time, temperature and ratio of the solvent affect the morphology of the NPs. The reaction carried out is depicted in schematically in figure 1.

2.3. Characterization techniques used

The crystal structure of the samples were examined using powder x-ray diffractometer (D8 Advance Bruker diffractometer) which employ Cu-Kα radiation with $\lambda = 1.5406$ Å. Debye–Scherrer equation was used to calculate the crystallite size of samples. The microstructural images were taken in a field emission scanning electron microscope (FESEM, FEI Quanta 200). The magnetic parameters were measured in the vibrating sample magnetometer (VSM, LakeShore). Fourier transform infrared (FTIR) spectrum were recorded in Shimadzu IR Prestige spectrometer. Magnetic induction heating experiments for all the samples were performed using Amberal EASYHEAT-8310, 4.2 kW system. For heating efficiency, different concentration of 0.5, 1 and 2 mg ml^{-1} of the NPs were dispersed in water and taken in vials, sonicated and placed in the AMF. The difference in temperature was measured using a optical fibre temperature sensor. The time versus temperature graphs were plotted and the initial slopes were calculated. SAR for the samples were estimated using the following equation (2)

$$SAR = C_{water} \times \frac{1}{m} \times \frac{\Delta T}{\Delta t} \qquad (2)$$

Where C_{water} is the specific heat of water with value of 4.2 J g^{-1} °C^{-1}, m is the mass of the NPs in aqueous suspension and $\Delta T/\Delta t$ is the initial slope of the temperature curve.

3. Results and discussion

3.1. Microstructural analysis

The XRD patterns for the prepared NPs are shown in figure 2(a). The diffraction peaks are indexed to the cubic phase of $MnFe_2O_4$ corresponding to JCPDS card No 00-010-0319. The high intensity peaks found at 2θ (in degree) values of 34.92, 42.51, 52.20, 56.04, 61.46, 64.42 and 72.44 are corresponding to the reflection planes (311), (400), (422), (511), (440), (531) and (533), respectively which suggests the formation cubic phase of $MnFe_2O_4$ NPs. The crystallite sizes of the samples were calculated using position of the highest intensity peak at
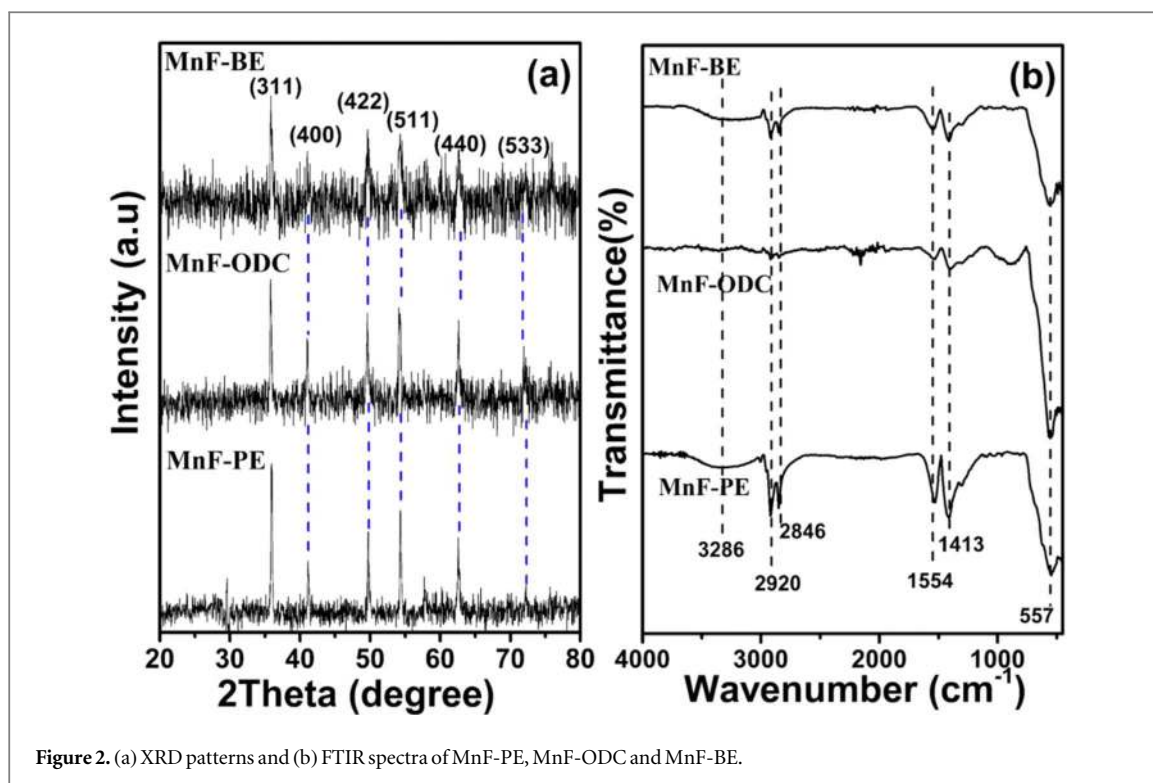
Figure 2. (a) XRD patterns and (b) FTIR spectra of MnF-PE, MnF-ODC and MnF-BE.

$34.92°$ and full width at half maximum intensity. The calculated crystallite sizes are found to be 9.0 nm, 11.5 nm and 10.2 nm for MnF-PE, MnF-BE and MnF-ODC respectively. Figure 2(b) shows the FTIR spectra of all the samples. The peak at 1413 cm^{-1} in all the spectra is referred to the symmetric COO$^-$ vibrations of oleic acid on NPs. The two vibrational bands in the range of 1400 cm^{-1} to 1600 cm^{-1} correspond to the N–H bending and C–N stretching modes of oleylamine, respectively [31]. This suggests the surface functionalization of oleic acid and oleylamine on the surface of all the samples. For MnF-ODC, an extra peak visible at 996 cm^{-1} indicates C=C bending of the alkene from the ODC solvent. The stretching modes of CH$_2$ and CH$_3$ present in oleylamine are observed in all the samples at 2846 cm^{-1} and 2920 cm^{-1}, respectively. The broad peak centred at 3286 cm^{-1} is attributed to the amine stretching vibration. The strong bands at 557 cm^{-1} indicate the metal oxide bond of octahedral and tetrahedral site compounds in the spinel structure of the samples.

For further confirmation of MnFe$_2$O$_4$ phase, XPS has been taken to confirm the oxidation states. XPS patterns of MnF-BE are shown in figure 3. The ferrite phase of MnFe$_2$O$_4$ is confirmed by the presence of two Fe^{2+} peaks at 709.98 and 723.86 eV of Fe 2p$_{1/2}$ and Fe 2p$_{3/2}$ respectively and presence of Mn^{2+} at 640.62 and 652.16 eV of Mn 2p$_{1/2}$ and Mn 2p$_{3/2}$, respectively [32]. The carbon C 1s peak at 283.1 eV is obtained by the organic molecule oleic acid and oleylamine present on the surface of the NPs. The XPS spectra of oxygen O 1s show a peak at 528 eV is due to the oxygen present in MnFe$_2$O$_4$. Thus XPS data of synthesized NP confirms the formation of pristine MnFe$_2$O$_4$ NPs.

The FESEM images and particle size distribution of MnF-PE, MnF-BE and MnF-ODC are shown in figure 4. The average particle size as obtained from FESEM images are 10 nm, 13 nm and 11 nm for MnF-PE, MnF-BE and MnF-ODC respectively are approximately in match with the crystallite sizes calculated from XRD. Generally, the size of the NPs linearly increases with the boiling temperature of the solvents showing the dependency of growth rate to the reaction temperature [16, 33]. However, in the present study, in case of BE, the NPs size are larger than the particles synthesized from ODC. This deviation in size shows the functional group of the solvent alters the stability and decomposition kinetics of iron complexes which affects the nucleation and growth rate of the NPs. By considering the LaMer model [17], the nucleation dependency on the solvent is shown in figure 4(d). The synthesis of NPs takes place by two steps nucleation and growth process. From figure 4(d), the barrier of the activation energy for nucleation is higher than the growth step. The burst nucleation takes place when concentration (C) is greater than C$_{min}$, where C$_{min}$ is the minimum monomer concentration required for nucleation. The higher monomer concentration occurs with the decomposition of precursors at higher temperatures. The radius of the stable nuclei formation is inversely proportional to the supersaturation. Thus at C $<$ C$_{max}$, where C$_{max}$ is the supersaturation of the monomer, a lesser amount of nuclei with larger radius are formed but with C $>$ C$_{max}$, a larger amount of nuclei with smaller radius are

Figure 3. XPS of MnF-BE NPs; (a) profile spectrum, (b) Mn 2p, (c) Fe 2p and (d) O 1s.
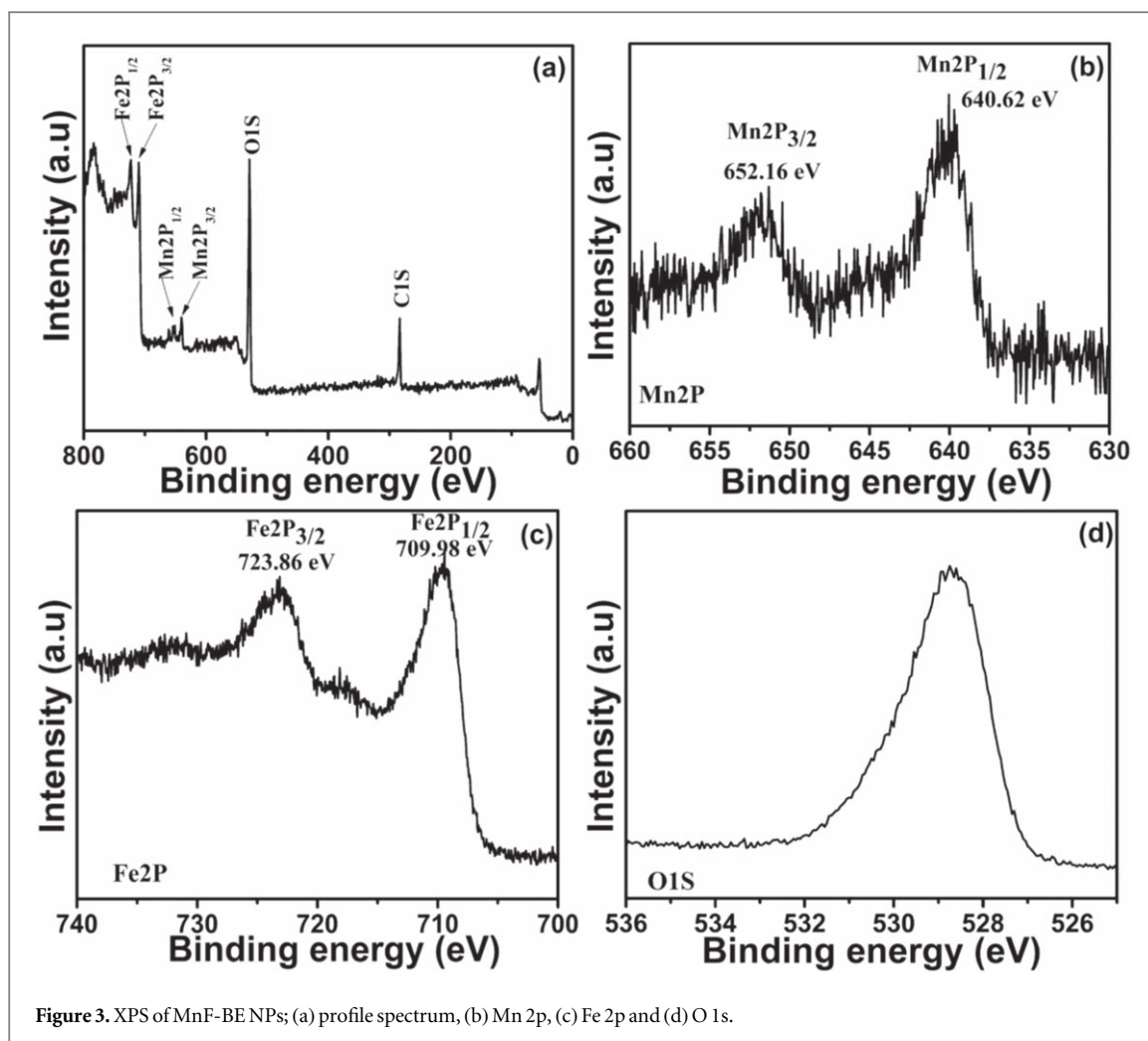
formed. The use of 1-octadecene at the higher temperature would be in agreement with higher C_{max} value and hence particles are formed with smaller radius [24]. The NPs synthesized with BE solvent show perfect cubic shape with the side length of 13 nm. It is well known that the shape of the particle can be varied by changing the oleic acid and oleylamine ratio in the reaction [25]. In the present study, all the synthesis parameters and reagents are kept fixed except for the use of different solvents. Thus, morphology also relies on the reductive environment in the thermal decomposition reaction. In general, BE acts as an antioxidant and hence, in the presence of oxygen it turns into benzaldehyde and benzoic acid that give a strong reductive environment when compared to other solvents. So, the monomer and nucleation formation in BE were much faster and the formed nucleation entered into kinetic growth phase earlier. In general, face-centred cubic (fcc) structure of spinel ferrite nanocrystal has three low-energy facets e.g. (100), (110), and (111). The highest surface energy possessed by the (111) planes and the growth along this leads to the formation of cubical nanostructures [34]. Thus bigger size cubic shaped NPs are formed in benzyl ether whereas for phenyl ether and 1-octadecene, the nucleation was dominant over the growth process resulting in smaller size spherical shaped NPs.

3.2. Magnetic properties

The magnetisation the samples at 300 K as the function of the applied magnetic field are shown in figure 5(a) with the inset graph showing the coercivity of the samples. The hysteresis behaviour of the NPs are consistent with nearly superparamagnetic behaviour. The samples MnF-PE, MnF-BE and MnF-ODC possessed M_s value of 42.0, 51.3 and 48.9 emu g^{-1} respectively. In agreement with previous studies [35–37], the Ms value are related to the size of the NPs. The lower Ms in smaller sized particles are associated with the surface spin disorder by excess long chain capping ligand attached directly on the surface or by the absence of some ions from the spinel lattice [38, 39]. The Ms values of the NPs are quite lower than the bulk $MnFe_2O_4$ which possesses Ms value of 80 emu g^{-1} [40]. Additionally, the coercivity Hc is decreasing with the increase in size. This can be supported with single domain particle theory proposed by Stoner and Wohlfarth [41] which shows Hc depends on both the Ms and anisotropy constant (K) given by the equation (3)
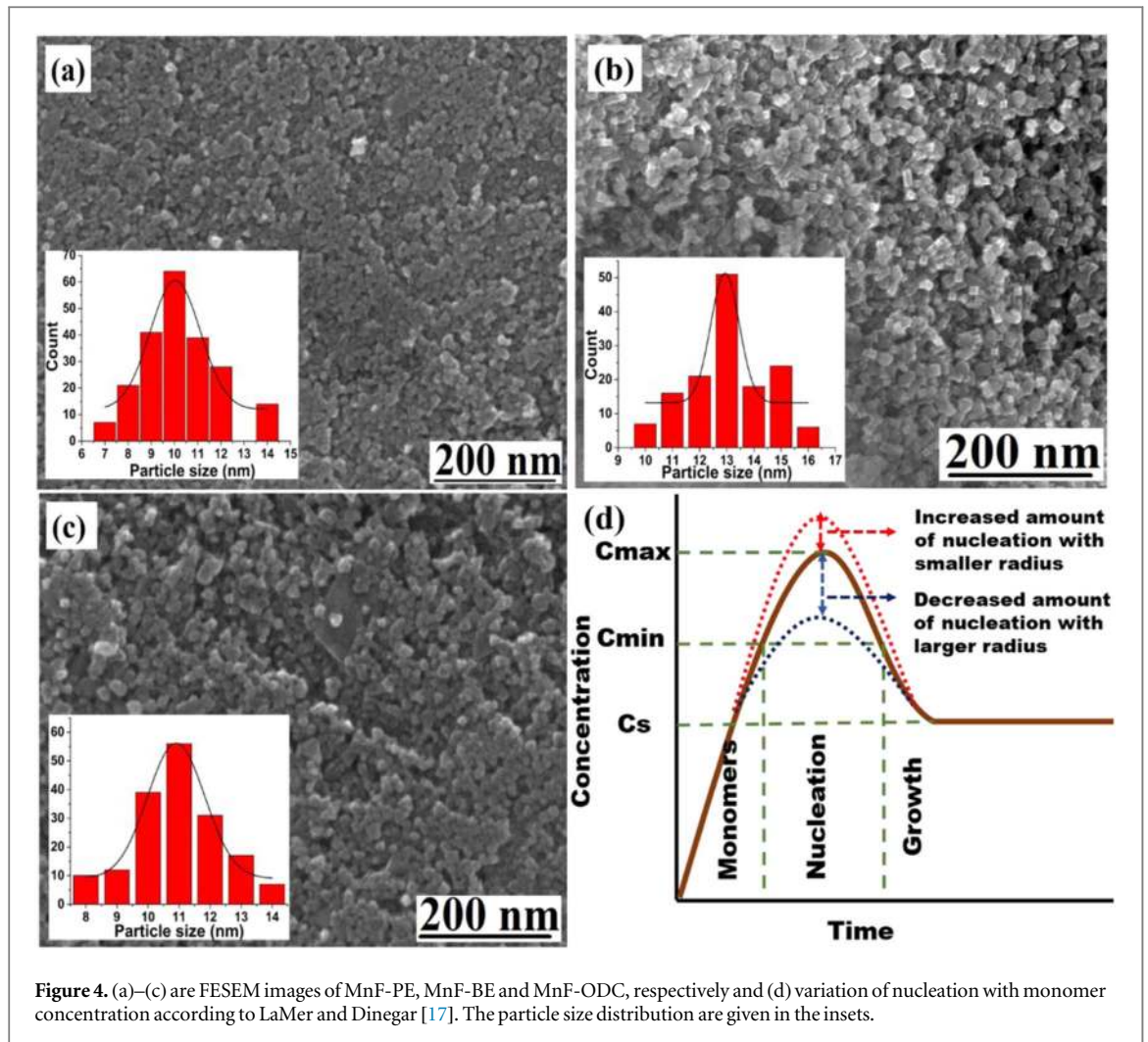
Figure 4. (a)–(c) are FESEM images of MnF-PE, MnF-BE and MnF-ODC, respectively and (d) variation of nucleation with monomer concentration according to LaMer and Dinegar [17]. The particle size distribution are given in the insets.
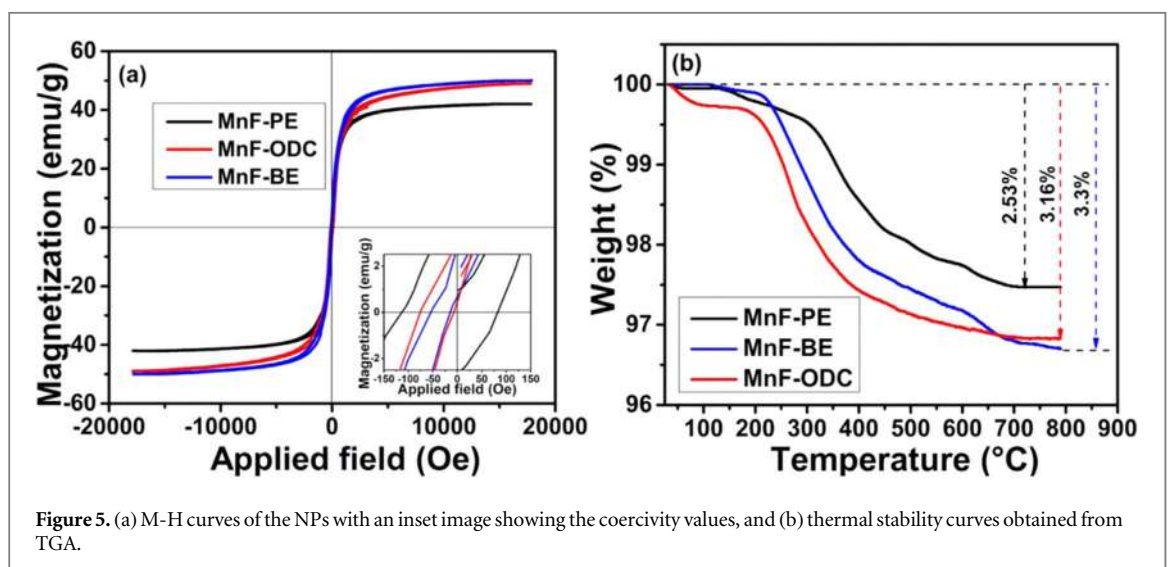
Figure 5. (a) M-H curves of the NPs with an inset image showing the coercivity values, and (b) thermal stability curves obtained from TGA.

$$Hc = \frac{2\,K}{\mu_o Ms} \tag{3}$$

Kahmei *et al* [42] reported the Ms value of 22 emu g^{-1} for 15 nm size MnFe$_2$O$_4$ particle by thermal decomposition method. Another study by Pal *et al* [43] reported MnFe$_2$O$_4$ particle of size 5 nm shows *Ms* value of 30 emu g^{-1}. The *Ms* value of 42 emu g^{-1} for 13 nm cubical MnF-BE is comparatively higher than the reported values.

3.3. Thermogravimetry analysis

Weight loss profile measurements were recorded from room temperature to 800 °C (figure 5(b)). TGA of $MnFe_2O_4$ NPs show weight loss of 2.5% to 3.3% when size varied from 9 nm to 13 nm. The materials are almost stable up to 200 °C without any loss. Weight loss observed from 200 to 450 °C is due to the decomposition of the oleic acid and oleylamine surfactants [44]. Since all the samples were prepared with the same weight of the precursors and volume of the surfactants, the ratio of surfactant coated on the NPs surface is proportional to the size of the NPs. The surface-to-volume ratio increases as the particle size decreases, and the surfactant amount on the surface decreases [45]. The weight loss profiles indicate the surface functionalization of the NPs which are highly stable in hydrophobic solvents such as hexane and toluene.

3.4. Magnetic hyperthermia

Magnetic hyperthermia heating application is based on Neel and Brownian motion of the magnetic NPs. In the presence of an applied AMF, the moment of magnetic particle rotates (Neel relaxation) as well as the particle itself rotates (Brownian relaxation) and relaxes back to normal orientation with the phase lag between the direction of magnetic moment and applied field. This phase lag relaxation process releases heat energy. The particle heating efficiency is calculated as specific loss power (SLP) or specific absorption rate (SAR). The SAR value of the particles should be higher for the safe application of magnetic hyperthermia in clinical uses. This is because the NPs with high SAR provide efficient heat generation at low concentration. By Rosenweig's theory, the heat generation depends on the parameters like frequency of the applied magnetic field, particle size, magnetization, magnetic anisotropy and viscosity of the solvent [46].

Clinically available NanoActivator(MagForceAG, Germany) operates at the applied field of 18 kA m^{-1} with a frequency of 100 kHz [47]. This low frequency is used to minimize the effect of generation of eddy current in the human body by Faraday's law. Till date, on maximum tolerable frequency and field, there is limited research and clinical data. Atkinson *et al* in 1984 proposed that the frequency and strength of the field applied cannot be increased beyond a certain limit (maximum frequency = 13.56 MHz or the product of frequency and field strength = 4.85×10^8 A ms^{-1}) in clinical trials for safety reasons [48]. However, in certain research, it is shown that this limit can be exceeded. Even in phase 1 and 2 trial of MagForce, patients with glioblastoma tolerate up to 13.5 kA m^{-1} whereas patients with prostate cancer tolerate till 5 kA m^{-1} [49, 50]. It is due to the difference in tissue conductivity and dielectric constant. Considering this, further research is required on the maximum tolerable limit of applied magnetic field strength and frequency.

Another major factor on which the magnetic hyperthermia highly depends is the concentration of the administered material in the tumour site. In a clinical trial, patients with glioblastoma cancer have been administered by magnetite NPs up to 31.36 mg of Fe/cm^3 [51]. The recommended dosage of FDA approved Feraheme (AMAG Pharmaceuticals, USA) is 510 mg [52]. Thus, heat generation by NPs in magnetic hyperthermia varied by some of the parameters such as magnetic field parameters (strength and frequency) and the concentration of the NPs in the colloid. Here, we have discussed and analysed the effect of two parameters field strength and concentration.

For studying the heating efficacy of the NPs, surface modified $MnFe_2O_4$ with Tetramethyl-ammonium 11-aminoundecanote is dispersed in water. The sample concentrations used for hyperthermia studies were 0.5, 1 and 2 mg ml^{-1}. For induction heating, 9 turns of 6 cm diameter coil is used with the applied field (Frequency = 314 kHz, Field strength = 375, 425, 475, 525 and 575 Oe). The hyperthermia temperature of 42 °C is reached by all the samples under different parameters were recorded by the fibre optic sensor. Figure 6 shows the linear increase in temperature with time under different field strength for all the samples at a concentration of 2 mg ml^{-1}. It is seen that with the rise in the applied field, the time required to reach the hyperthermic temperature decreases. The hyperthermic behaviour is directly proportional to the magnetic parameters of the NPs. MnF-BE NPs requires less time to reach the temperature under different field and different concentration when compared with MnF-ODC and MnF-PE. This may be due to the high *Ms* value and cubic shape of the particles since the cubic shaped particle poses high anisotropy value as compared to the spherical shape. The SAR values calculated from the initial slope obtained from the time versus temperature graph for all concentrations at different applied fields are given in figure 7. The high SAR value was possessed by all the NPs from different solvents. The maximum SAR value was obtained by MnF-BE is 438 W g^{-1} at a concentration of 2 mg ml^{-1} and with an applied field of 575 Oe compared to other NPs might be due to the cubic shape. This is a high SAR value than the reported literature [42, 53]. These results prove that the degree of induced heat by the NPs can be controlled by the concentration and applied field and indicates the suitability of these NPs in magnetic hyperthermia application.
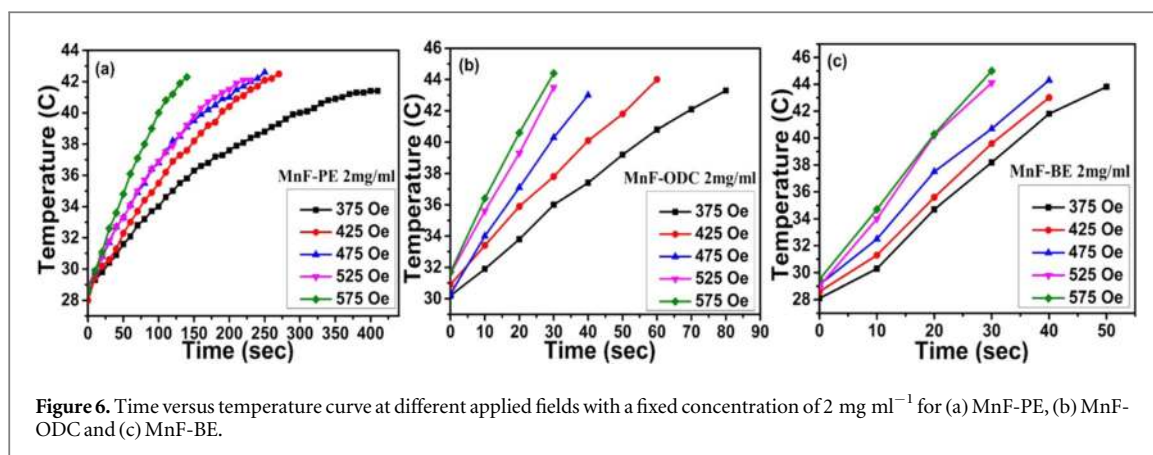
Figure 6. Time versus temperature curve at different applied fields with a fixed concentration of 2 mg ml^{-1} for (a) MnF-PE, (b) MnF-ODC and (c) MnF-BE.
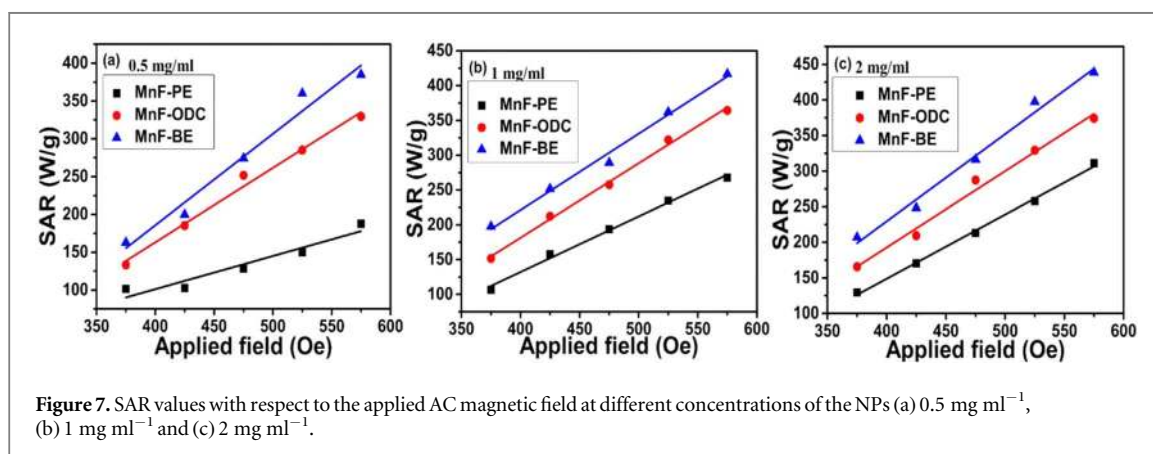

Figure 7. SAR values with respect to the applied AC magnetic field at different concentrations of the NPs (a) 0.5 mg ml^{-1}, (b) 1 mg ml^{-1} and (c) 2 mg ml^{-1}.

4. Conclusion

In summary, the simple thermal decomposition method with different high boiling solvent can be used to synthesis high quality MnFe$_2$O$_4$ with different morphology. The dual functioning role of solvents as reducing agents also proved from the different shapes of the NPs obtained. By keeping the reagents and surfactants ratio as constant, the heating rate or boiling point of the solvents determine the size and shape of the particles. The synthesized particle MnF-PE and MnF-ODC show nearly spherical shape whereas the particle synthesized in BE MnF-BE shows cubic shape. The ligand exchange process by Tetramethyl-ammonium 11-aminoundecanote produces highly stable hydrophilic NPs. The potential of these synthesized NPs as magnetic hyperthermia agent shows better SAR values when compared with most of the research data and commercial agents. The SAR efficiency of NPs is size and morphology dependent. These stable NPs with superior magnetic properties can be utilized as hyperthermia agent for cancer therapy.

Acknowledgments

ORCID iDs

Niroj Kumar Sahu ⦿ https://orcid.org/0000-0002-0499-4108

References

[1] Cheon J *et al* 2004 Shape evolution of single-crystalline iron oxide nanocrystals *JACS* **126** 1950–1
[2] Kim D *et al* 2009 Synthesis of uniform ferrimagnetic magnetite nanocubes *J. Am. Chem. Soc.* **131** 454–5
[3] Yin Y and Alivisatos A P 2005 Colloidal nanocrystal synthesis and the organic-inorganic interface *Nature* **437** 664–70.

[4]   Eustis S and el-Sayed M A 2006 Why gold nanoparticles are more precious than pretty gold: noble metal surface plasmon resonance and its enhancement of the radiative and nonradiative properties of nanocrystals of different shapes *Chem. Soc. Rev.* **35** 209–17

[5]   Jun Y W, Choi J S and Cheon J 2006 Shape control of semiconductor and metal oxide nanocrystals through nonhydrolytic colloidal routes *Angew. Chem. Int. Ed. Engl.* **45** 3414–39

[6]   Rao C N *et al* 2012 Recent progress in the synthesis of inorganic nanoparticles *Dalton Trans.* **41** 5089–120

[7]   Dobson J 2008 Remote control of cellular behaviour with magnetic nanoparticles *Nat. Nanotechnol.* **3** 139–43

[8]   Lee N *et al* 2015 Iron oxide based nanoparticles for multimodal imaging and magnetoresponsive therapy *Chem. Rev.* **115** 10637–89

[9]   Laurent S *et al* 2008 Magnetic iron oxide nanoparticles: synthesis, stabilization, vectorization, physicochemical characterizations, and biological applications *Chem. Rev.* **108** 2064–110

[10] Kumar S *et al* 2013 *In vitro* evaluation of PEGylated mesoporous MgFe$_2$O$_4$ magnetic nanoassemblies (MMNs) for chemo-thermal therapy *J. Mater. Chem.* B **1** 3652–60

[11] Sahu N K, Gupta J and Bahadur D 2015 PEGylated FePt-Fe$_3$O$_4$ composite nanoassemblies (CNAs): *in vitro* hyperthermia, drug delivery and generation of reactive oxygen species (ROS) *Dalton Trans.* **44** 9103–13

[12] Kumar S R *et al* 2014 Hydrophilic polymer coated monodispersed Fe$_3$O$_4$ nanostructures and their cytotoxicity *Mater. Res. Express* **1** 015015

[13] Prasad A I *et al* 2013 Bi-functional properties of Fe3O4@YPO4:Eu hybrid nanoparticles: hyperthermia application *Dalton Trans.* **42** 4885–96

[14] Kim D-H *et al* 2009 T1 and T2 relaxivities of succimer-coated MFe$_2^{3+}$ O$_4$ (M = Mn^{2+}, Fe^{2+} and Co^{2+}) inverse spinel ferrites for potential use as phase-contrast agents in medical MRI *J. Magn. Magn. Mater.* **321** 3899–904

[15] Kim J H *et al* 2008 Mangafodipir trisodium-enhanced MRI of hepatocellular carcinoma: correlation with histological characteristics *Clin. Radiol.* **63** 1195–204

[16] Park J *et al* 2004 Ultra-large-scale syntheses of monodisperse nanocrystals *Nat. Mater.* **3** 891–5

[17] LaMer V K and Dinegar R H 1950 Theory, production and mechanism of formation of monodispersed hydrosols *JACS* **72** 4847–54

[18] Hyeon T *et al* 2001 Synthesis of highly crystalline and monodisperse maghemite nanocrystallites without a size-selection process *J. Am. Chem. Soc.* **123** 12798–801

[19] Sun S and Zeng H 2002 Size-controlled synthesis of magnetite nanoparticles *JACS* **124** 8204–5

[20] Diab M and Mokari T 2014 Thermal decomposition approach for the formation of α-Fe$_2$O$_3$ mesoporous photoanodes and an α-Fe$_2$O$_3$/CoO hybrid structure for enhanced water oxidation *Inorg. Chem.* **53** 2304–9

[21] Kovalenko M V *et al* 2007 Fatty acid salts as stabilizers in size-and shape-controlled nanocrystal synthesis: the case of inverse spinel iron oxide *JACS* **129** 6352–3

[22] Sun S *et al* 2004 Monodisperse MFe$_2$O$_4$ (M = Fe, Co, Mn) Nanoparticles *JACS* **126** 273–9

[23] Jović Orsini N *et al* 2018 Magnetic and power absorption measurements on iron oxide nanoparticles synthesized by thermal decomposition of Fe(acac)$_3$ *J. Magn. Magn. Mater.* **449** 286–96

[24] Baaziz W *et al* 2014 Magnetic iron oxide nanoparticles: reproducible tuning of the size and nanosized-dependent composition, defects, and spin canting *The J. Phys. Chem.* C **118** 3795–810

[25] Lu L T *et al* 2015 Synthesis of magnetic cobalt ferrite nanoparticles with controlled morphology, monodispersity and composition: the influence of solvent, surfactant, reductant and synthetic conditions *Nanoscale* **7** 19596–610

[26] Zhou Z *et al* 2015 Anisotropic shaped iron oxide nanostructures: controlled synthesis and proton relaxation shortening effects *Chem. Mater.* **27** 3505–15

[27] Wetterskog E *et al* 2014 Precise control over shape and size of iron oxide nanocrystals suitable for assembly into ordered particle arrays *Sci. Technol. Adv. Mater.* **15** 055010

[28] Cotin G *et al* 2018 Unravelling the thermal decomposition parameters for the synthesis of anisotropic iron oxide nanoparticles *Nanomaterials* (Basel, Switzerland) **8** 881

[29] Venkatesha N *et al* 2016 ZnO coated CoFe$_2$O$_4$ nanoparticles for multimodal bio-imaging *RSC Adv.* **6** 18843–51

[30] Bronstein L M *et al* 2007 Influence of iron oleate complex structure on iron oxide nanoparticle formation *Chem. Mater.* **19** 3624–32

[31] Hergt R and Dutz S 2007 Magnetic particle hyperthermia—biophysical limitations of a visionary tumour therapy *J. Magn. Magn. Mater.* **311** 187–92

[32] Venkatesha N *et al* 2015 MnFe$_2$O$_4$–Fe$_3$O$_4$ core–shell nanoparticles as a potential contrast agent for magnetic resonance imaging *RSC Adv.* **5** 97807–15

[33] Demortière A *et al* 2011 Size-dependent properties of magnetic iron oxide nanocrystals *Nanoscale* **3** 225–32

[34] de Faria D L A, Venâncio Silva S and de Oliveira M T 1997 Raman microspectroscopy of some iron oxides and oxyhydroxides *J. Raman Spectrosc.* **28** 873–8

[35] Caruntu D, Caruntu G and O'Connor C J 2007 Magnetic properties of variable-sized Fe$_3$O$_4$ nanoparticles synthesized from non-aqueous homogeneous solutions of polyols *J. Phys. D: Appl. Phys.* **40** 5801–9

[36] Li Q *et al* 2017 Correlation between particle size/domain structure and magnetic properties of highly crystalline Fe$_3$O$_4$ nanoparticles *Sci. Rep.* **7** 9894

[37] Smolensky E D *et al* 2013 Scaling laws at the nano size: the effect of particle size and shape on the magnetism and relaxivity of iron oxide nanoparticle contrast agents *J. Mater. Chem.* B **1** 2818–28

[38] Goya G F *et al* 2003 Static and dynamic magnetic properties of spherical magnetite nanoparticles *J. Appl. Phys.* **94** 3520–8

[39] Berkowitz A E *et al* 1999 Anomalous properties of magnetic nanoparticles *J. Magn. Magn. Mater.* **196-197** 591–4

[40] Bozorth R M, Tilden E F and Williams A J 1955 Anisotropy and magnetostriction of some ferrites *Phys. Rev.* **99** 1788–98

[41] Stoner E C and Wohlfarth E P 1948 A mechanism of magnetic hysteresis in heterogeneous alloys *Philosophical Transactions of the Royal Society of London. Series A, Mathematical and Physical Sciences* **240** 599–642

[42] Ralandinliu Kahmei R D and Borah J P 2018 Clustering of MnFe$_2$O$_4$ nanoparticles and the effect of field intensity in the generation of heat for hyperthermia application *Nanotechnology* **30** 035706

[43] Pal M, Rakshit R and Mandal K 2014 Surface modification of MnFe$_2$O$_4$ nanoparticles to impart intrinsic multiple fluorescence and novel photocatalytic properties *ACS Applied Materials & Interfaces* **6** 4903–10

[44] Sahu N K, Prakash A and Bahadur D 2014 Role of different platinum precursors on the formation and reaction mechanism of FePt nanoparticles and their electrocatalytic performance towards methanol oxidation *Dalton Trans.* **43** 4892–900

[45] Krishna Surendra M *et al* 2014 Magnetic hyperthermia studies on water-soluble polyacrylic acid-coated cobalt ferrite nanoparticles *J. Nanopart. Res.* **16** 2773

[46] Rosensweig R E 2002 Heating magnetic fluid with alternating magnetic field *J. Magn. Magn. Mater.* **252** 370–4

[47] Jordan A *et al* 2001 Presentation of a new magnetic field therapy system for the treatment of human solid tumors with magnetic fluid hyperthermia *J. Magn. Magn. Mater.* **225** 118–26

[48] Atkinson W J, Brezovich I A and Chakraborty D P 1984 Usable frequencies in hyperthermia with thermal seeds *IEEE Trans. Biomed. Eng.* **BME-31** 70–5

[49] Johannsen M *et al* 2007 Morbidity and quality of life during thermotherapy using magnetic nanoparticles in locally recurrent prostate cancer: results of a prospective phase I trial *Int. J. Hyperth.* **23** 315–23

[50] Maier-Hauff K *et al* 2007 Intracranial thermotherapy using magnetic nanoparticles combined with external beam radiotherapy: results of a feasibility study on patients with glioblastoma multiforme *J. Neurooncol.* **81** 53–60

[51] Maier-Hauff K *et al* 2011 Efficacy and safety of intratumoral thermotherapy using magnetic iron-oxide nanoparticles combined with external beam radiotherapy on patients with recurrent glioblastoma multiforme *J. Neurooncol.* **103** 317–24

[52] Lu M *et al* 2010 FDA report: ferumoxytol for intravenous iron therapy in adult patients with chronic kidney disease *Am. J. Hematol.* **85** 315–9

[53] Cruz M M *et al* 2017 Enhanced magnetic hyperthermia of $CoFe_2O_4$ and $MnFe_2O_4$ nanoparticles *J. Alloys Compd.* **703** 370–80